



**HAL**  
open science

# Experimental and numerical study of combining encapsulated phase change material to sensible heat storage material in one-tank pilot scale thermal energy storage

Muhammad Asaad Keilany, Ségolène Vannerem, Mathieu Milhé, Quentin Falcoz, Jean-Jacques Bézian, Gilles Flamant

## ► To cite this version:

Muhammad Asaad Keilany, Ségolène Vannerem, Mathieu Milhé, Quentin Falcoz, Jean-Jacques Bézian, et al.. Experimental and numerical study of combining encapsulated phase change material to sensible heat storage material in one-tank pilot scale thermal energy storage. *Journal of Energy Storage*, 2022, 51, pp.104504. 10.1016/j.est.2022.104504 . hal-03637554

**HAL Id: hal-03637554**

**<https://imt-mines-albi.hal.science/hal-03637554>**

Submitted on 21 Apr 2022

**HAL** is a multi-disciplinary open access archive for the deposit and dissemination of scientific research documents, whether they are published or not. The documents may come from teaching and research institutions in France or abroad, or from public or private research centers.

L'archive ouverte pluridisciplinaire **HAL**, est destinée au dépôt et à la diffusion de documents scientifiques de niveau recherche, publiés ou non, émanant des établissements d'enseignement et de recherche français ou étrangers, des laboratoires publics ou privés.

# Experimental and numerical study of combining encapsulated phase change material to sensible heat storage material in one-tank pilot scale thermal energy storage

M.A. Keilany<sup>a,b,\*</sup>, S. Vannerem<sup>b</sup>, M. Milhé<sup>a</sup>, Q. Falcoz<sup>b</sup>, J.-J. Bézian<sup>a</sup>, G. Flamant<sup>b</sup>

<sup>a</sup> Centre RAPSODEE, Université de Toulouse, Ecole des Mines d'Albi, CNRS, Albi F-81013, France

<sup>b</sup> CNRS-PROMES, 7 Rue du Four Solaire, 66120 Font Romeu-Odeillo, France

## A B S T R A C T

### Keywords:

One-tank thermal energy storage  
Enthalpy porosity method  
Sensible heat  
Latent heat storage  
Phase change material  
Concentrated solar power plant

This work presents the design, experimental and numerical results related to a pilot-scale one-tank (thermocline) thermal energy storage (TES) combining latent and sensible heat storage materials with synthetic oil as heat transfer fluid (HTF). The layer of phase change material (PCM) is used to enhance the thermal performance of the TES. Alumina spheres are used as sensible heat storage materials, while the PCM is NaNO<sub>3</sub> (sodium nitrate). The PCM is encapsulated inside 140 stainless steel tubes. The volume of the PCM represents 5.5% of the storage volume. NaNO<sub>3</sub> was found safe to use with the synthetic oil at the designated operating conditions in case of leaks in the tank. The influence of the phase change material on HTF temperatures were observed experimentally during charge, discharge and stand-by. A numerical model that couples two one-dimensional (1D) physical methods is developed. It simulates natural convection within the PCM capsules by modifying the thermal conductivity of the material. The enthalpy porosity method is applied to simulate the phase changing behavior and a single equation estimates the liquid fraction of the PCM at each time step. The model is validated from the experimental results. This validation reveals that there is still a high fraction of unsolidified PCM in the tubes during discharge, which indicates that the performance of the combined TES solution is limited by heat transfer within the encapsulation tubes.

## 1. Introduction

Concentrated solar power (CSP) is one of the promising renewable energies that could help countries achieving their green energy production goals. One of the main advantages of CSP plants is the ability to store energy on a large scale using thermal energy storage (TES) to provide 24 h a day operation [1]. Among the three TES solutions, sensible heat, latent heat, and thermo-chemical heat storage, CSP plants are generally using only sensible heat storage [2]. Kuravi et al. [3] showed that the most commercially developed storage technology in CSP plants is the two-tank molten salts sensible TES. Py et al. [1] concluded that about 49% of the two-tank TES cost is attributed to the molten salts.

One-tank also known as (Thermocline) TES could be an economically viable TES solution in CSP plants because it replaces a two-tank TES system with a single tank. Moreover, it uses inexpensive filler materials and decreases the need for expensive HTF. J.E. Pacheco et al. [4] concluded that a one-tank TES filled with quartzite rocks and operated

with molten salts as HTF costs only 66% of the total investment of two tanks installation that uses molten salts as a storage medium and as HTF. However, during the charge and discharge process of the TES, a thermal gradient layer, typically called the thermocline thickness (or region), develops between the hot and cold zones of the tank. The quality of stored and released energy degrades inside this region, because the fluid will be at a temperature lower than the useful temperature [5]. While this layer is expanding during the charge and discharge operations, it could account for up to 33% of total tank height [6], which reduces the storage efficiency of the system and influences the outlet temperature of the HTF flowing out the TES.

Phase change material (PCM) has a unique capacity to store/release thermal energy at a relatively constant temperature. Therefore, it attracted the attention in different engineering fields, such as temperature control applications and TES. Table 1 summarizes various PCM applications appeared in the literature [7–11].

Adding a layer of PCM to a sensible heat TES tank could help stabilizing the HTF outlet temperature due to quasi constant heat release/

\* Corresponding author at: Centre RAPSODEE, Université de Toulouse, Ecole des Mines d'Albi, CNRS, Albi F-81013, France.

E-mail address: [makeilany@outlook.com](mailto:makeilany@outlook.com) (M.A. Keilany).

Nomenclature	
$\alpha_s$	Shape factor [ $m^2/m^3$ ]
$A_{f \rightarrow w}$	Area of heat exchange between HTF and tank's wall [ $m^2$ ]
$C_p$	Heat capacity [Joul/kg.k]
$d$	Filler diameter [m]
$D$	Tank diameter [m]
$e_{tube}$	Tube thickness [m]
$e_w$	Tank wall thickness [m]
$e_{ins}$	Insulation layer thickness [m]
$\hat{G}$	Non-dimensional quantity derived from the discretization of the PCM equation [m]
$H$	Height [m]
$h_{air}$	convection heat transfer coefficient between tank's wall and surrounding atmosphere [ $w/m^2.K$ ]
$h_{env}$	convection heat transfer coefficient between tube's wall and HTF [ $w/m^2.K$ ]
$h_{f-p}$	convection heat transfer coefficient between HTF and filler materials [ $w/m^2.K$ ]
$h_v$	Volumetric convection heat transfer coefficient between HTF and Solid filler particles [ $w/m^3.K$ ]
$h_w$	convection heat transfer coefficient between HTF and tank's wall [ $w/m^2.K$ ]
$k_{f,eff}$	Effective thermal conductivity of HTF [ $w/m.K$ ]
$k_{f-ax}$	Axial effective thermal conductivity of HTF in the D—C model [ $w/m.K$ ]
$k_{pcm-eff}$	Effective thermal conductivity of PCM [ $w/m.K$ ]
$k_{p,eff}$	Effective thermal conductivity of Solid filler particles [ $w/m.K$ ]
$l_{ch}$	Characterize length [m]
$L_{fus}$	Laten heat of fusion [Kj/kg]
$m$	Mass [kg]
$\dot{m}$	Mass flow rate [kg/s]
$\mu$	Dynamic viscosity [kg/m.s]
$\nu$	kinematic viscosity [ $m^2/s$ ]
$P_{max}$	Maximum allowable internal pressure [ $N/m^2$ ]
$r$	Radius [m]
$r_i$	Control volume at the radial axis of the tube [m]
$SE$	Maximum allowable stress [ $N/m^2$ ]
$T$	Temperature [K]
$T_{z,t}$	Temperature at axial position z at time t [K]
$TS$	Tensile strength of the material [ $N/m^2$ ]
$t$	Time [sec]
$U_c$	The combined uncertainty % [—]
$u_i$	The individual uncertainty source% [—]
$V$	Volume [ $m^3$ ]
$v_f$	Local velocity of HTF [ $m/s$ ]
$z$	Axial coordinate [m]
<i>Greek symbols</i>	
$\beta$	The coefficient of thermal expansion [1/K]
$\epsilon$	Tank porosity (void fraction) [—]
$\rho$	Density [ $kg/m^3$ ]
$\theta$	Non dimensional temperature [—]
$\lambda$	Liquid fraction [—]
<i>Subscripts</i>	
<b>env.</b>	Encapsulation
<b>f</b>	Heat transfer fluid
<b>Melt</b>	Phase changing material melting point
<b>p</b>	Solid filler particles
<b>PCM</b>	Phase change material
<b>w</b>	Tank wall
<b>liq.</b>	Liquefied phase change material
<b>sol.</b>	Solidified phase change material
<b>in</b>	Inner tank diameter
<b>out</b>	Outer tank diameter
<b>ins</b>	Insulated tank diameter
<i>Superscript</i>	
<b>n</b>	time reference
<b>j</b>	Positions reference in axial direction
<b>*</b>	Non dimensional quantity

**Table 1**  
Diverse PCM applications [7–11].

Hot and cold TES
<ul style="list-style-type: none"> <li>• TES with heat pumps.</li> <li>• Full-size PCM storage.</li> <li>• Multilayered PCM storage.</li> <li>• Combine PCM with other types of TES: sensible or thermochemical.</li> <li>• Solar TES with heat pumps: for building applications.</li> </ul>
Temperature control
<ul style="list-style-type: none"> <li>• Cooling management of electronic chips.</li> <li>• Space heating and cooling. Integrated into building structure and components.</li> <li>• Protection and thermal management to batteries and vehicles.</li> <li>• Protection of delicate electronic components.</li> <li>• Protection of sensitive medical products.</li> <li>• Thermal control of transportation for food and beverages.</li> <li>• Use for personnel human needs, such as vests, clothes, hot, and cold local treatments.</li> <li>• Thermal control of photovoltaic panels (PV), or combined photovoltaic-thermal applications (PVT).</li> </ul>

store during the phase change [12]. Furthermore it could improve the thermal performance of the TES at a low cost [13]. Few studies addressed this question to the authors' best knowledge, and experimental data allowing validation of modelling approaches in these

studies are scarce.

Hernández et al. [14] numerically investigated a combined PCM layer of AlSi positioned above a sensible heat storage material (SHSM) of steel slag the HTF operates between 27 and 597 °C and the phase change temperature of the PCM is 576 °C. They applied one-dimensional (1D) Continuous-Solid model (C-S) model on both latent and sensible heat layer in the storage to study the effect of PCM ratio on the storage performance. The study concluded that the optimum design is with a 5% volume fraction of PCM layer when comparing 0%, 1%, 2.5%, 5%, 10%, and 20%.

Galione et al. [15–17] evaluated the concept of a three-layer one-tank TES using 1D Dispersion-Concentric (D-C) model; 20% of KOH380 as a PCM at the top, 60% of quartz rocks and sand as SHSM at the middle, and 20% of KOH300 as a PCM at the bottom. The operating temperatures of the suggested storage are 290–390 °C. Their simulations showed better TES efficiency in the three-layered concept compared to the case without PCM.

Zhao et al. [18] developed a numerical tool to study a 2000 MWh<sub>th</sub> TES, using a 1D D-C model. They compared various setups with the same thermal storage capacity: one-tank 100% SHSM filler, one-tank 100% PCM, one-tank 50% low temperature (LT) PCM + 50% high temperature (HT) PCM, multilayer one-tank 10% LT-PCM+ 80% SHSM+10% HT-PCM, and two-tanks sensible heat storage. They suggested a methodology to design a one-tank TES. Moreover, they concluded that using the multilayer solution requires a smaller tank size than the sensible heat only, and provides the best replacement to the two-tanks TES compared

to other evaluated solutions.

Zanganeh et al. [12] numerically studied the influence of the PCM layer size when combined to a rocks-filled one-tank TES that operates between 590 and 650 °C. They tested three PCMs with four different volume fraction of 0% PCM (sensible heat only), 0.67% PCM, 1.33% PCM, and 2.67% PCM. The model is 1D with C-S approach in both layers; sensible and PCM. They concluded that 1.33% of PCM stabilized the outlet temperature of the tank for the simulated PCMs and provided the best discharge efficiencies between the evaluated cases.

In another study of the same team, Zanganeh et al. [19] performed an experimental work that combined PCM to SHSM in a 42 kWh<sub>th</sub> lab-scale one-tank TES, the sensible heat part being filled with rocks, and the latent heat part with AlSi<sub>12</sub>. The PCM is contained inside a bundle of stainless-steel tubes placed in staggered positions, where the PCM volume ratio to the tank's height is 1.33%. The storage works between 20 and 600 °C and the PCM melting temperature is 575 °C. A C-S model is validated from the experimental results and used to compare the discharge process of the combined solution to sensible heat storage only. It is shown that the discharge lasted for about 28.5% longer with this combination compared to the sensible heat TES tank, with more stable outlet temperature around the PCM melting point.

Ahmed et al. [13] used the one-dimensional (1D) Schumann model to compare three setups of one-tank TES. The first is filled only with solid rod structures as low-cost SHSM, the second contains only PCM spheres, and the third combines the two. The operating temperature range is 135–195 °C, and the melting temperature of the PCM is 165 °C. They found that the combined solution has a lower cost compared to the PCM only TES and better performance compared to the sensible heat only TES.

Although PCM integration in a one-tank TES provides a performance enhancement opportunity, it is still not widely used in commercial installations. In order to improve confidence and reliability on the solution, some challenges need further research and analysis, such as the thermal behavior, output temperature stability, safety, and materials issues. Furthermore, a reliable modelling tool is required, as well as pilot-scale experimental and operational results.

This work presents an experimental and modelling study of a combining PCM layer to SHSM in a pilot-scale one-tank TES in a micro CSP plant. The work addresses design challenges such PCM material selection, encapsulation, and safety issues to build this solution at a pilot-scale size. A compatibility test is performed between synthetic oil (HTF) and NaNO<sub>3</sub> (PCM) to ensure no fire in case of accidental leakage. In addition, it provides 1D simulation method that couples two physical models for each layer, the C–S in the SHSM layer and D–C in the PCM layer. The objective is to have fast and reliable numerical solutions that address the limitations of each approach. In the following, the

experimental setup is firstly presented as well as the material issues. The numerical models for both the sensible and the PCM layer are then detailed. The last section (before the conclusion) addresses the experimental results and their comparison with the numerical data. It includes a discussion on melting fraction in the PCM tubes. The PCM melting/solidification is simulated using enthalpy porosity method (EPM), where an equation for estimating the liquid fraction in the PCM is expressed according to Voller method [20]. Moreover, the model simulates natural convection inside the PCM capsules by modifying the thermal conductivity of the PCM during the phase change.

## 2. Experimental setup

### 2.1. MICROSOL-R facility

The main experiments of this study were performed with the MICROSOL-R setup of PROMES laboratory (Font-Romeu-Odeillo-Via, France). Fig. 1 illustrates the MICROSOL-R facility [21].

During the charging process, valve V4 is opened while the charge pump P1 is activated allowing the synthetic oil HTF to be heated by a 70 kW electrical heater (EH). The three way valve V2 is opened in the tank direction and valve V3 is opened to charge the one-tank TES (TC) while valve V5 is closed.

For the discharge, the valve V4 is closed, and the discharge pump P2 starts injecting cold HTF in the tank TC from the bottom. The hot HTF exits the tank from its top, V5 is opened and valve V3 is closed. The HTF is cooled down using three water-steam heat exchangers HEX1, HEX2, and HEX3. The outlet temperature of HEX3; which represents the inlet temperature of the TES, can be controlled using four parameters: the water pump power P3, and the opening percentage of the valves V6, V7, and V8. The water is cooled down using a water-glycol-cooled heat exchanger HEX4 operated by the pump P4, where the heat is rejected to the surrounding atmosphere using three air fans.

The thermal energy storage TC is a 4 m<sup>3</sup> tank, 3.24 m height and 1.276 m internal diameter shown on Fig. 2. The tank contains four vertically positioned baskets allowing easy access to the solid storage material while filling and emptying. Furthermore, these baskets reduce the possibility of thermal ratcheting.

The tank contains two buffer zones that include tubular HTF distributors enabling a homogeneous HTF distribution (see distributors on Fig. 3).

The solid bed height is 2.64 m, and thermocouples are used to record HTF temperature every 2 s with a precision of ±1.5 °C. They are distributed in the axial and radial positions, as illustrated in Fig. 4.

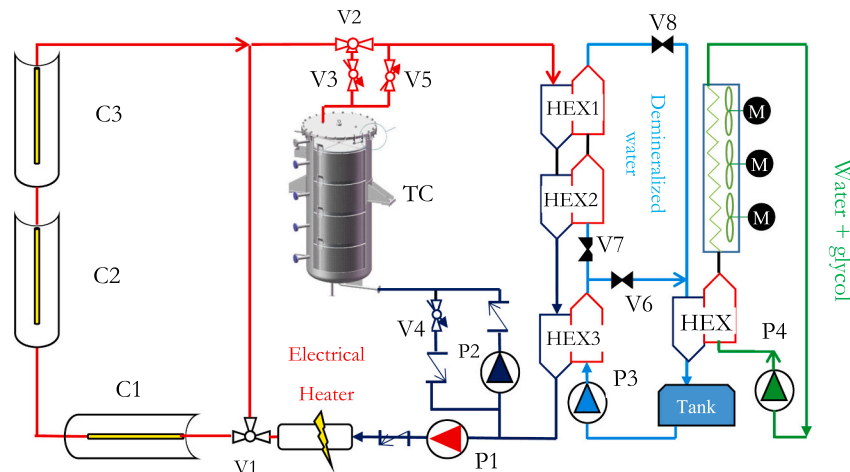


Fig. 1. Schematic of Microsol-R pilot plant.

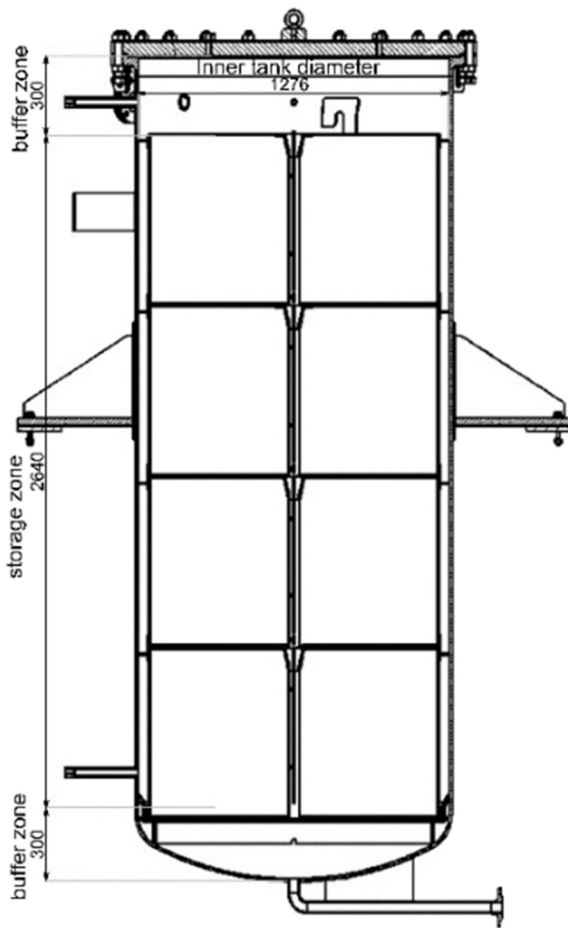


Fig. 2. TES at the Microsol-R.



Fig. 3. HTF distributor at the top of the tank.

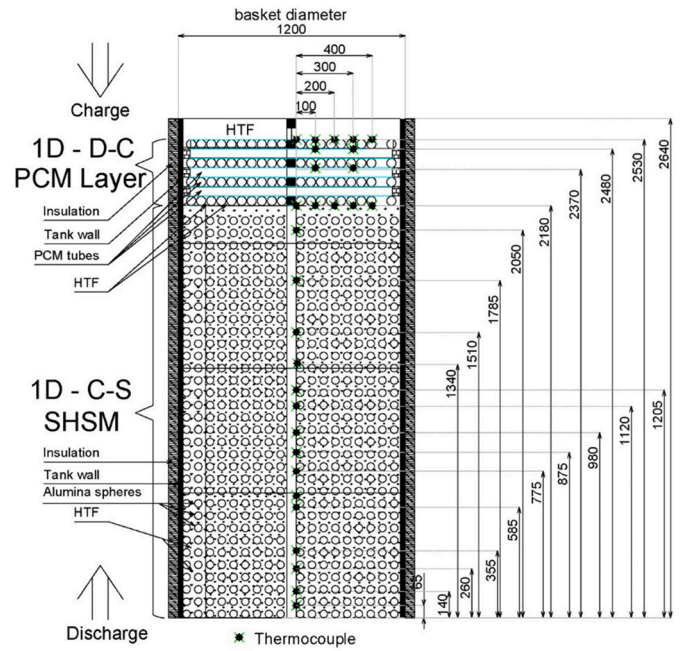


Fig. 4. The storage zone inside the tank size and thermocouple positions.

## 2.2. Operational limitations and experimental conditions

The preferred operating temperature defined by the original design is between 220 and 315 °C the HTF is a synthetic oil that has a working temperature range of 0–350 °C. The system shuts off completely if the temperature exceeds 345 °C at any point in circuit for safety reason.

It is not possible to perform a charge process with a large temperature difference between the inlet and the outlet of the TES tank in one-step in this work. Mainly due to the electrical-heater power limitation, for example, we cannot inject HTF at 315 °C, while the HTF within the TES tank is at 225 °C. Hence, the charge must be performed in three successive stages to achieve the targeted 315 °C temperature starting from 220 °C. The focus of this work is on the final charging step between 286 and 315 °C, because it contains the melting phase of the PCM.

Table 2 illustrates the TES tank inlet/outlet temperature and the mass flow rate for a typical charge/discharge process. These operating conditions are applied in the experiment as well as the numerical study.

## 2.3. Thermal energy storage materials

The sensible heat storage material is 2 cm in diameter alumina spheres that fills the lower part of the tank and has a mass of 4.66 tons. The same materials was used in our previous work inside MICROSOL-R [5].

The chosen PCM is sodium nitrate  $\text{NaNO}_3$ , with a melting temperature of 306 °C [22,23]. It is available on the local market at a relatively low price and suitable purity >99% [24]. Furthermore, it has proven compatibility with Stainless steel 304 L, which is an excellent candidate material for the envelope.

The latent heat of fusion of sodium nitrate was measured using a differential scanning calorimetry (DSC). A 65.66 mg sample was heated at a constant rate of 10 °C/min from 30 °C up to 400 °C and then cooled

Table 2  
Operating conditions.

Process	Charge	Discharge
Mass flow rate [kg/h]	2700	2000
Temperature range [°C]	286–315	312–226

down at the same rate. The heat flow curve from the DSC in Fig. 5 confirms that latent heat of fusion of NaNO<sub>3</sub> is about 169 kJ/kg, and the material melts at 307 °C and solidifies at 304.3 °C.

For the encapsulation material, Stainless steel SS304 is chosen because it meets the criteria of envelope selection for PCM application as compiled in Table 3 from [8,25–28].

Furthermore, Goods et al. [29] confirmed that the SS304 metal shows a decay rate is 6–15 μm/year when using a mixture of NaNO<sub>3</sub> and KNO<sub>3</sub> at 570 °C. This low rate of degradation of SS304 with NaNO<sub>3</sub> qualifies it to be used for long term service [8] with NaNO<sub>3</sub> at a working temperature of 350 °C [3,30].

Thermo-physical properties of all involved materials are calculated as follow:

- HTF Jarytherm® oil [According to product technical datasheet].

$$\rho = 1261.569 - 0.7419173 \cdot T(\text{K}).$$

$$C_p = 649.84 + 3.1872180451 \cdot T(\text{K}).$$

$$k = 0.1521663 - 8.2406015038 \cdot 10^{-5} \cdot T(\text{K}).$$

$$\mu = \exp.[19.75102 \cdot (\ln T(\text{K}))^4 - 492.2114 \cdot (\ln T(\text{K}))^3 + 4602.039 \cdot (\ln T(\text{K}))^2 - 19,136.34 \cdot (\ln T(\text{K})) + 29,858.54].$$

$$\rho = 1000 \cdot (3.9853 - (7.158 \cdot 10^{-5} \cdot T(^{\circ}\text{C})) - (3.035 \cdot 10^{-8} \cdot T(^{\circ}\text{C})^2) + (7.232 \cdot 10^{-12} \cdot T(^{\circ}\text{C})^3)).$$

- Alumina spheres [31,32]

$$C_p = 1117 + 0.14 \cdot T(\text{K}) - 411 \cdot \exp.(-0.006 \cdot T(\text{K})).$$

$$k = -2.469 \cdot 10^{-8} \cdot T(\text{K})^3 + 9.509 \cdot 10^{-5} \cdot T(\text{K})^2 - 0.124 \cdot T(\text{K}) + 61.76.$$

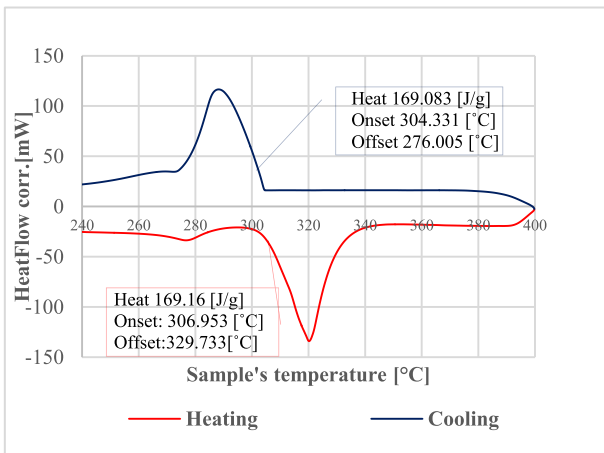


Fig. 5. DSC results for the commercial NaNO<sub>3</sub>.

Table 3

Required specifications for proper PCMs envelop design [8,25–28].

Mechanical stability and flexibility	- Withstand internal pressure resulting from density differences between phases. - Provide the required structural rigidity. - Allow easy PCM filling in, easy to manufacture.
Thermal stability	- Sustain the maximum working temperature. - Adapt to extension/contraction due to thermal cycling, with a compatible thermal expansion coefficient.
Compatibility	- Corrosion resistance to PCM as well as HTF at the predetermined temperature.
Integrity	- Prevent the PCM from interacting with the surrounding atmosphere.
Sufficient heat transfer coefficient.	- Provide a significant effective heat transfer coefficient, suitable shape, and thermal conductivity.

- Stainless steel 304 L

$$\rho = 8030 \text{ [kg/m}^3\text{]}.$$

$$C_p = 502.48 \text{ [kJ/kg.K]}.$$

$$k = 16 \text{ [W/m.K]}$$

- NaNO<sub>3</sub> [33]

$$\rho_{\text{liquid}} = 2160 \text{ [kg/m}^3\text{]}.$$

$$\rho_{\text{solid}} = 1908 \text{ [kg/m}^3\text{]}.$$

$$C_p = 444.53 + 2.18 \cdot T(\text{K}).$$

$$k = 0.3057 + 4.47 \cdot 10^{-4} \cdot T(\text{K}).$$

$$L_{\text{fus}} = 169 \text{ [kJ/kg]}.$$

## 2.4. Safety analysis

The main concern when using the NaNO<sub>3</sub> with the synthetic oil Jarytherm® DBT is fire issue because sodium nitrate is considered “class I oxidizers” that is the minimum out of four hazard classes [34], and oil is a fuel. Therefore, two analyses were performed to ensure a low level of risk in case of crack in the metal envelope. The first one aims to evaluate the integrity of the tube to withstand the internal pressure from the PCM density variation between solid to liquid and thus minimizing the potential leakage. The second one evaluates the just-in-case scenario of accidentally mixing the two materials.

### 2.4.1. Internal pressure

The maximum allowable internal pressure for a cylindrical container can be calculated from hoop stress Eq. (1) [35].

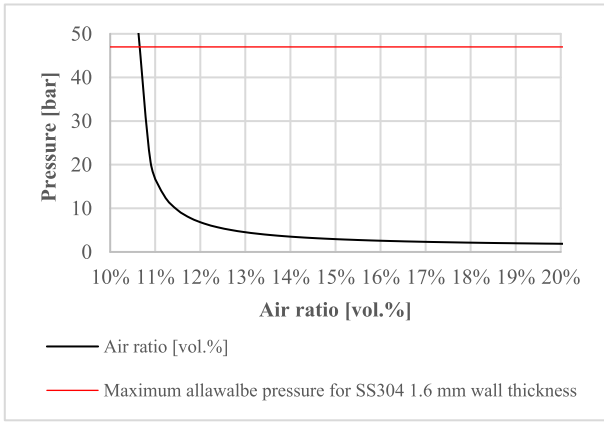


Fig. 6. Internal pressure versus air ratios of NaNO<sub>3</sub> fill SS304 48.3/45.1 tube.

$$P_{max} = 2 \cdot SE \cdot \frac{e_{tube}}{d_{env}} \quad (1)$$

$e_{tube}$ : the thickness of the tube.

SE: is the maximum allowable stress for the materials.

SE = 0.85 TS/4: TS: tensile strength of the material.

From Eq. (1), a 48.3 mm outer diameter, 1.6 mm thickness SS304 tube can tolerate up to 47 bar. The maximum pressure expected inside the container due to the density difference between the solid and the liquid phase is estimated from Eq. (2) [36], which neglects the envelope material thermal expansion.

$$P_{max} = P_{atm} \left( \frac{V_{void} - \frac{m_{PCM}}{\rho_{sol}}}{V_{void} - \frac{m_{PCM}}{\rho_{liq}}} \right) \quad (2)$$

An air volume is suggested allowing the PCM to expand without stressing the tube wall. The air ratio is defined as the ratio of air volume to the inner volume of the encapsulation expressed in vol% at normal conditions.

Fig. 6 plots the internal pressure within a 48.3 mm outer diameter SS304 tube of 1.6 mm thickness against air ratio. It confirms that a minimum of 10.7% air ratio is necessary to avoid exceeding the maximum allowable pressure for this type of tube [37]. Therefore, an air volume of 14% of the internal tube volume is chosen for this work.

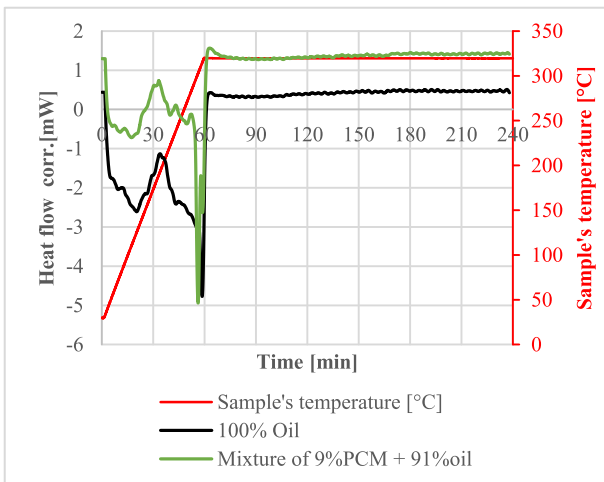


Fig. 7. DSC Heat flow comparison between 100% Oil and 91%wt.Oil-9%wt.NaNO<sub>3</sub>.

#### 2.4.2. Compatibility between NaNO<sub>3</sub> and synthetic oil

Pacheco et al. [4] evaluated the behavior of a mixture of Therminol® HTF and liquid NaNO<sub>3</sub>. They concluded that there is no fire risk when mixing this oil and NaNO<sub>3</sub>, furthermore, any fire incident primary cause would be mixing the hot oil vapor with oxygen from the air, while “accidentally mixing the two components should not create combustion”. Moreover, NaNO<sub>3</sub> is thermally stable with a harmless formation of nitrite (NaNO<sub>2</sub>) and Oxygen (O<sub>2</sub>) at 380 °C at atmospheric pressure [37,38]. Moreover, the leading cause of nitrate salts explosion is ascribed to the ammonium nitrate (NH<sub>3</sub>NO<sub>3</sub>) and not to NaNO<sub>3</sub> or KNO<sub>3</sub> [34].

Although no direct contact between the PCM and oil is ensured in this experiment by using stainless-steel pipes with a proper sealing method, the reactivity of mixing NaNO<sub>3</sub> with Jarytherm® oil was investigated experimentally with two analyses. The first simulates an arbitrary small PCM leakage into the HTF with a weight ratio of 9% NaNO<sub>3</sub> to 91% oil, while the second depicts a small quantity of oil leaching inside the PCM encapsulation with a weight ratio of 84% NaNO<sub>3</sub> to 16% oil (filling the air gap within the tubes with oil).

Fig. 7 compares the heat flow measurements of differential scanning microscopy (DCS) for the 100% oil reference sample which contained 49.67 mg of oil, to the 91 wt% oil- 9 wt% NaNO<sub>3</sub> mixture sample with total weight of 45.31 mg. The temperature was increased at a constant rate of 5 °C/min up to 320 °C, then maintained at the highest temperature for 180 min for both experiments.

Fig. 7 illustrates that the two curves have very similar shape, and no peaks are observed at the heat flow curve during the test. The difference between the two curves is attributed to additional thermal capacity of the NaNO<sub>3</sub> as well as its latent heat of fusion. The mixture curve shows some deviation from the reference sample at a temperature around 300 [°C] which could be explained by the melting of the PCM.

For the second analysis, the two tested samples are 109.08 mg of 100% NaNO<sub>3</sub>, and 61.72 mg consists of 16 wt% oil and 84 wt% NaNO<sub>3</sub>. The DCS parameters are the same applied in the first analysis. Fig. 8 compares the heat flow between the two samples, where the shape of the two curves are also very similar, and no peaks in the heat flow are detected. Moreover, the 100% PCM sample has a bigger overall heat than the mixed sample due to its bigger mass as well as the latent heat of fusion of the PCM compared to the mixture sample, where the oil is introduced.

Figs. 7 and 8 indicate that there are no exothermic reactions during these analyses, which confirms that there is no fire risk from mixing a small amount of NaNO<sub>3</sub> to the Jarytherm® oil or a small amount of oil to

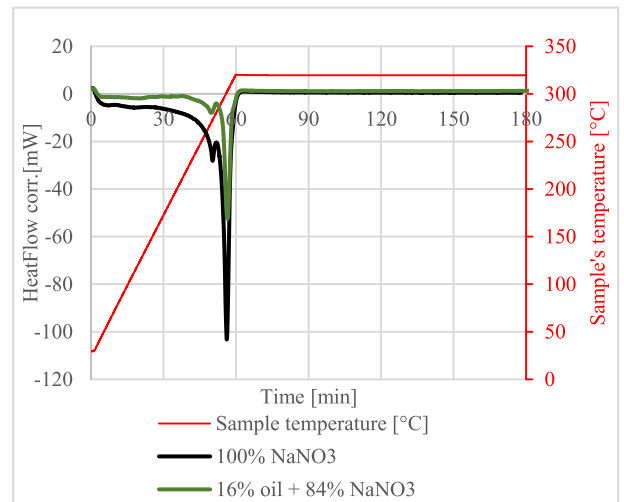


Fig. 8. DSC measurements of 100% NaNO<sub>3</sub> and a mixture of 86%wt. NaNO<sub>3</sub>-16% wt.Oil.

**Table 4**  
PCM mass, envelope mass, envelope volume, and filling ratio for each row.

Row	$m_{env}$ [kg]	$m_{PCM}$ [kg]	$V_{tube}$ [m <sup>3</sup> ]	Filling ratio
1	34.72	48.12	0.031	86.63%
2	34.72	48.25	0.031	86.86%
3	34.71	48.07	0.031	86.51%
4	34.72	48.29	0.031	86.87%
5	34.72	48.21	0.031	86.78%
6	34.70	48.10	0.031	86.59%
7	34.69	48.21	0.031	86.80%
Total	242.98	337.24	0.22	



**Fig. 9.** The final PCM layer package.

NaNO<sub>3</sub> at a temperature up to 320 [°C].

### 2.5. PCM layer design

For this experimental work, a 5.5% volumetric ratio of PCM to the total tank volume is chosen. The PCM layer consists of 7 rows of SS304 tubes 48.3 mm outer diameter. Each tube is side-sealed on one side by welded end-cap, while the other tube side is closed with a threaded end-cap with suitable sealant material for high temperature applications. The final measured porosity of the PCM layer is 0.508.

The tubes are filled using several stages as follows: 1- Measure the tare weight of the empty tubes. 2- Fill vertically the salt inside the tubes. 3- Place the vertical tubes in an electric furnace to melt the PCM that results in extra space formation (This step ensures no leakage from the bottom of the tubes). 4- Add more PCM in the tubes and repeat steps 3 and 4 until reaching the required PCM filling ratio inside the tube. 5- Record the tubes' gross weight. 6- Seal the tubes with Deacon 770-P® (high-temperature tube's sealant) and a copper washer. 7- Place the tubes horizontally inside the furnace and subject the containers to 3 cycles of melting/solidification. 8- Inspect visually for any possible leakages. 9- Check each tube for hidden leakages by comparing its gross weight before and after cycling.

The filling details of PCM layer is reflected in **Table 4**, which shows for each row: the mass of filled PCM ( $m_{PCM}$ ), the mass of stainless steel ( $m_{env}$ ), the volume of tubes ( $V_{tube}$ ), and the average filling ratio.

The final arrangement of tubes in the PCM layer is illustrated in **Fig. 9**.

### 2.6. Uncertainty of measurements

The combined standard uncertainty of measurements is evaluated using the root-sum-square method of all associated uncertainties Eq. (3) [30].

$$P_{max} = P_{atm} \left( \frac{V_{void} - \frac{m_{PCM}}{\rho_{sol}}}{V_{void} - \frac{m_{PCM}}{\rho_{liq}}} \right) \quad (3)$$

$U_c$ : is the combined uncertainty.

$u_i$ : is the individual uncertainty source.

The experimental setup has PYRO-SYSTEM® thermocouples type PT100 1/3 B, which have  $\pm 0.6$  °C uncertainty, by neglecting the uncertainty of data acquisition switch, this results in 1.2% uncertainty in temperature reading relative to 100 °C temperature difference. Moreover, each thermocouple has a position uncertainty of  $\pm 2.5$  cm that will give 1.9% uncertainty relative to 2.64 m total tank height. The mass flow-metering device (Foxboro® Model 84F) has  $\pm 0.5\%$  uncertainty of measurement. Applying Eq. (3) gives 9.8% of combined uncertainty.

Uncertainties in the temperature dependence of alumina thermophysical properties are estimated at 2% for heat capacity and 6% for thermal conductivity [31]. NaNO<sub>3</sub> has an uncertainty of 6% in the measured thermophysical properties [39]. Therefore, the combined uncertainty equation of the NaNO<sub>3</sub> as PCM and alumina spheres as solid filler in one tank is about 13%.

### 3. Numerical model

Biot number ( $Bi$ ) of the solid filler is calculated from in accordance to Eq. (4). Where the characterized length  $L_{ch}$  is  $d/6$  for a sphere, and  $d/4$  for a tube [40].

$$P_{max} = P_{atm} \left( \frac{V_{void} - \frac{m_{PCM}}{\rho_{sol}}}{V_{void} - \frac{m_{PCM}}{\rho_{liq}}} \right) \quad (4)$$

For the heat convection coefficient  $h_{f-p}$ , Nusselt number ( $Nu$ ) is calculated from the correlation suggested by Wakao et al. [41] Eq. (5).

$$P_{max} = P_{atm} \left( \frac{V_{void} - \frac{m_{PCM}}{\rho_{sol}}}{V_{void} - \frac{m_{PCM}}{\rho_{liq}}} \right) \quad (5)$$

The flow regime is evaluated by calculating  $Re$  at the particle diameter level for a randomly packed bed from Eq. (6) [42].

$$P_{max} = P_{atm} \left( \frac{V_{void} - \frac{m_{PCM}}{\rho_{sol}}}{V_{void} - \frac{m_{PCM}}{\rho_{liq}}} \right) \quad (6)$$

The numerical model of this work uses a 1D Continuous-Solid

**Table 5**  
Biot number of alumina spheres and NaNO<sub>3</sub> tubes at 315/220 °C and 2600 kg/h mass flow rate.

Material	Bed porosity	Temperature [K]	Diameter [m]	$Re$	$Bi$
Alumina	0.485	493.15	0.02	35.17	0.023
NaNO <sub>3</sub>	0.508		0.048	88.34	1.468
Alumina	0.485	588.15	0.02	65.73	0.032
NaNO <sub>3</sub>	0.508		0.048	165.11	1.706

approach (C–S) in the sensible heat storage part of the tank (alumina spheres) and a 1D Dispersion-Concentric (D–C) approach in the PCM layer of  $\text{NaNO}_3$  shown on Fig. 4. The C–S approach is used in the alumina spheres because  $Bi$  is inferior to 0.1, while in the PCM tube is superior to 0.1 Table 5. Moreover, the HTF flow in both parts of the tank; the alumina spheres and PCM tubes could be assumed laminar based on calculated  $Re$  values at the operating limits of this experiment based on the  $Re$  value calculated in Table 5, where  $Re < 260$  for random packed bed [43].

The simulation uses experimental tank inlet temperatures as model input with a constant mass flow rate at each process of charge and discharge. Table 2 indicates the maximum and minimum temperatures with the rates of charge and discharge used in the designated experiments.

### 3.1. One-dimensional continuous-solid model for sensible storage section

The main advantage of using the 1D C–S approach is performing a quick simulation within the largest part of the TES tank (the sensible heat storage with solid filler) with a good accuracy. The height of this part is 2.18 m.

#### 3.1.1. Model assumptions

- 1D incompressible HTF flow in the axial direction of the tank.
- The HTF flow is laminar as indicated in Table 5 [44].
- Heat transfer by radiation is neglected, because the maximum HTF temperature inferior to 660 °C [45].
- The solid is a continuous, isotropic porous medium.
- The temperature gradient within the 2 cm alumina sphere is negligible because  $Bi < 0.1$ .
- The tank is not adiabatic. Thermal losses to the environment are considered by solving the energy balance equation at the tank's walls.
- The model neglects the thermal conduction between the tank wall and solid filler.
- Thermal diffusion of the HTF in the axial direction is considered.
- The model uses temperature-dependent thermophysical properties.

#### 3.1.2. Energy balance equations

The Model solves three coupled energy balance equations in the HTF, solid filler, and wall temperature profiles, Eqs. (7)–(9), respectively.

For the fluid:

$$\varepsilon(\rho C_p)_f \frac{\partial T_f}{\partial t} + \varepsilon(\rho C_p)_f v_f \frac{\partial T_f}{\partial z} = k_{f,eff} \frac{\partial^2 T_f}{\partial z^2} + h_v(T_p - T_f) + h_w \frac{A_{f \leftrightarrow w}}{V_{\text{tank}}} (T_w - T_f)$$

$$A_{f \leftrightarrow w} = \varepsilon \cdot \pi \cdot D_{in} \cdot H_{\text{tank}} \quad (7)$$

For the solid particle:

$$(1 - \varepsilon)(\rho C_p)_p \frac{\partial T_p}{\partial t} = k_{p,eff} \frac{\partial^2 T_p}{\partial z^2} + h_v(T_f - T_p) \quad (8)$$

For the wall:

$$(\rho C_p)_w \frac{\partial T_w}{\partial t} = k_w \frac{\partial^2 T_w}{\partial z^2} + h_w \left( \frac{A_{f \leftrightarrow w}}{V_w} (T_f - T_w) \right) + \frac{(hA)_{w \leftrightarrow ext}}{V_w} (T_{ext} - T_w) \quad (9)$$

#### 3.1.3. Correlations

Eqs. (10) and (11) express the effective thermal conductivities of the fluid and the solid particle [5]:

$$k_{f,eff} = \varepsilon k_f \quad (10)$$

$$k_{p,eff} = (1 - \varepsilon) k_p \quad (11)$$

Eq. (12) calculates the volumetric heat convection coefficient [6]:

$$\frac{h_v}{h_{f-p}} = a_s \quad (12)$$

The shape factor (1/m) identified by the total surface area of all particles divided by the total volume of the tank [41], it is defined by Eq. (13):

$$a_s = \frac{A(\text{tot})_p}{V_{\text{tank}}} = \frac{v_p}{L_{ch}} = \frac{v_{\text{tank}} - v_f}{v_{\text{tank}}} = \frac{v_{\text{tank}} \left( 1 - v_f/v_{\text{tank}} \right)}{L_{ch}} \quad (13)$$

$$a_s = \frac{(1 - \varepsilon)}{L_{ch}}$$

And Eq. (14) evaluates the characteristic length for a spherical particle,  $L_{ch}$ :

$$L_{ch} \stackrel{\text{def}}{=} \frac{\text{Volume}}{\text{Area}} = \frac{d_p}{6} \quad (14)$$

Based on Eqs. (5), (12)–(14), the volumetric heat convection coefficient is calculated from Eq. (15), which is the mostly used correlation for spherical solid filler in modelling thermocline TES [44].

$$h_v = \frac{6(1 - \varepsilon) k_{f,eff} \left[ 2 + 1.1 Re_p^{0.6} Pr^{1/3} \right]}{d_p^2} \quad (15)$$

The convection heat transfer coefficient between HTF and the tank wall is calculated from Eq. (16) according to Beek [46]. This correlation is suitable to use with spherical and cylindrical filler when  $Re$  is inferior to 2000.

$$h_w = \frac{k_f}{d_p} \left( 2.576 Re_p^{1/2} Pr^{1/3} + 0.0936 Re_p^{0.8} Pr^{0.4} \right) \quad (16)$$

$$Re_p < 2000$$

The term  $(hA)_{w \leftrightarrow ext}$  is calculated from the equivalent thermal resistance of the cylindrical tank wall Eq. (17) [47].

$$\frac{1}{(hA)_{w \leftrightarrow ext}} = \sum R_{th} = R_{th,w} + R_{th,ins} + R_{th,air}$$

$$\frac{1}{(hA)_{w \leftrightarrow ext}} = \frac{\ln \left( \frac{D_{out}}{D_{in}} \right)}{2 \cdot \pi \cdot k_w \cdot H_{\text{tank}}} + \frac{\ln \left( \frac{D_{ins}}{D_{out}} \right)}{2 \cdot \pi \cdot k_{ins} \cdot H_{\text{tank}}} + \frac{1}{h_{air} \cdot A_{ext}} \quad (17)$$

$$D_{out} = D_{in} + 2e_w$$

$$D_{ins} = D_{in} + 2e_w + 2e_{ins}$$

$$A_{ext} = \pi \cdot (D_{in} + 2e_w + 2e_{ins}) \cdot H_{\text{tank}}$$

The heat convection coefficient at the outside tank wall is estimated from Eq. (18) according to Churchill et al. [48]. Where  $Nu$  of natural convection is valid for laminar as well as turbulent flow.

$$\frac{H_{\text{tank}} h_{air}}{k_w} = Nu_{air} = \left[ 0.825 + \frac{0.387 Ra_{air}^{1/4}}{\left( 1 + \left\{ \frac{0.492}{Pr_{air}} \right\}^{9/16} \right)^{1/4}} \right]^2 \quad (18)$$

$$Ra \leq 10^{12}$$

$$Pr = Cp \cdot \mu / k, Ra = Gr \cdot Pr, Gr = g \beta \Delta T H_{ch}^3 / \nu^2$$

Rayleigh number ( $Ra$ ) at the outside surface of the vertical tank is calculated from equation Eq. (19):

$$Ra_{air} = \rho_{air} g \beta_{air} H_{\text{tank}}^3 (T_{avg} - T_{ext}) / \nu \quad (19)$$

$\beta$  is the coefficient of thermal expansion (1/T for an ideal gas).

Air properties are taken at an average temperature  $T_{avg}$  between surrounding temperature  $T_{ext}$  and wall temperature  $T_w$ .

### 3.1.4. Initial conditions

During charge at time  $t = 0$ :

$$T_f^{(t=0)} = T_p^{(t=0)} = T_w^{(t=0)} = T_{initial}^{(t=0)} = T_{Low}$$

For discharge at  $t = 0$ :

$$T_f^{(t=0)} = T_p^{(t=0)} = T_w^{(t=0)} = T_{initial}^{(t=0)} = T_{High}$$

## 3.2. One-dimensional dispersion-concentric model for latent storage section

The calculated  $Bi$  for a tube diameter 48.3 mm filled with  $NaNO_3$  at 315 °C is between 1.4 and 1.7 Table 5, which emphasizes the need to use a numerical approach that considers the thermal gradient within the tube, hence the D–C approach is selected.

### 3.2.1. Model assumptions

- 1D incompressible HTF flow in the axial direction of the tank.
- Laminar flow, as justified in Table 5 [44].
- Heat transfer by radiation is neglected with maximum HTF temperature below 660 °C [45].
- The PCM is encapsulated in horizontal tubes.
- The temperature gradient within the PCM is assumed symmetric-concentric distributed.
- The thermal resistance of the stainless-steel tube is neglected due to its high thermal conductivity.
- The thermal capacity of the envelop materials is embedded in the thermal capacity of the PCM as defined by Eq. (20) [19].

$$(\rho Cp)_{eff} = \frac{m_{PCM} C_{p_{PCM}} + m_{env} C_{p_{env}}}{V_{Tubes}} \quad (20)$$

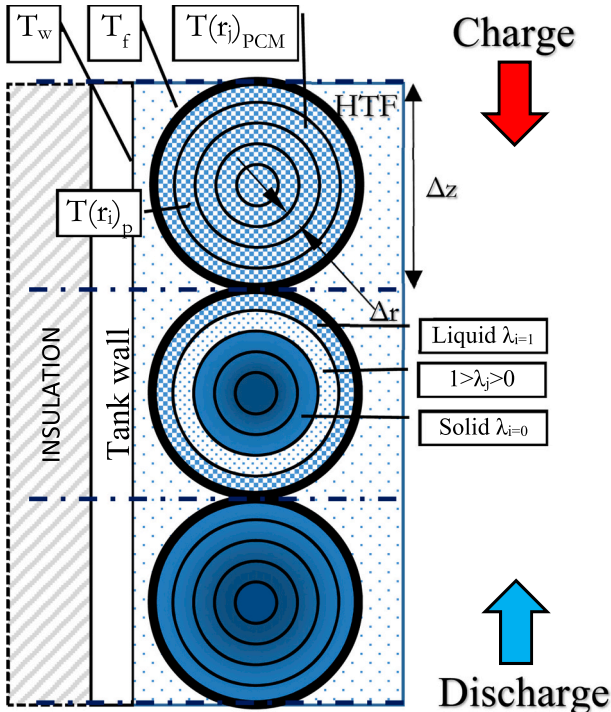


Fig. 10. The D–C model control volume of PCM layer.

- Natural convection of the PCM is simulated by modifying the thermal conductivity of the PCM during the phase change process according to Eq. (21) [49,50].

$$\frac{k_{pcm-eff}}{k_{PCM}} = 0.18 Ra_{PCM}^{0.25} \quad (21)$$

$$Ra_{PCM} = \rho_{PCM} g \beta_{PCM} d_{tube}^3 (T_f - T_m) / \nu_{PCM}$$

- The tank is not adiabatic, thus thermal losses to the environment are taken into account by solving the energy balance equation at the tank wall and adding a convective heat flux condition at the border.
- Conduction between the tank wall and the tubes is neglected.
- HTF thermal diffusion in the axial direction is considered.
- The model uses temperature-dependent thermophysical properties for the HTF and PCM.
- Melting and solidification of PCM are modeled using the enthalpy porosity method, which assumes a constant melting temperature during the phase change.
- $\lambda$  is the liquid fraction of the PCM, its value varies between zero and one and can be calculated with the enthalpy-porosity method.

### 3.2.2. Energy balance equations

The three coupled energy balance equations for the HTF, PCM, and wall temperature profiles Eqs. (22)–(24), respectively are solved according to the control volume presented in Fig. 10.

For the HTF:

$$\varepsilon(\rho Cp)_f \frac{\partial T_f}{\partial t} + \varepsilon(\rho Cp)_f v_f \frac{\partial T_f}{\partial z} = k_{f-ax} \frac{\partial^2 T_f}{\partial z^2} + h_{v,tube} (T_{pcm} - T_f) + h_w \frac{A_{f \leftrightarrow w}}{V_{tank}} (T_w - T_f) \quad (22)$$

For the PCM tubes:

$$(\rho Cp)_{pcm} \frac{\partial T_{pcm}}{\partial t} + \rho_{pcm} L_{fus} \frac{\partial \lambda}{\partial t} = \frac{1}{r} \frac{\partial}{\partial r} \left( k_{pcm} r \frac{\partial T_{pcm}}{\partial r} \right) \quad (23)$$

And for the tank wall:

$$(\rho Cp)_w \frac{\partial T_w}{\partial t} = k_w \frac{\partial^2 T_w}{\partial z^2} + h_w \left( \frac{A_{f \leftrightarrow w}}{V_w} (T_f - T_w) \right) + \frac{(hA)_{w \leftrightarrow ext}}{V_w} (T_{ext} - T_w) \quad (24)$$

The liquid fraction in the PCM equations is evaluated from Eq. (25) according to Voller [20] enthalpy porosity source term.

$$\lambda^{(r_j,n)^{k+1}} = \lambda^{(r_j,n)^k} - \frac{C_{p_{pcm}}^{(r_j,n)} \hat{G} \cdot (T_{melt} - T_{pcm}^{(r_j,n)})}{L_{fus}} \quad (25)$$

$$\begin{cases} \lambda^{(r_j,n)^{k+1}} < 0 \rightarrow : \lambda^{(r_j,n)^{k+1}} = 0 \\ \lambda^{(r_j,n)^{k+1}} > 1 \rightarrow : \lambda^{(r_j,n)^{k+1}} = 1 \end{cases}$$

$\hat{G}$  : is a non-dimensional quantity derived from the discretization of the PCM equation according to Eq. (26).

$$\hat{G} = 1 + \frac{\Delta t}{\Delta r} \frac{2}{r_j} \frac{k_{pcm}}{(\rho Cp)_{pcm}} \quad (26)$$

### 3.2.3. Correlations

Shape factor of the tube can be calculated from Eq. (27) [19].

$$L_{ch} \frac{def}{Area} : \text{for tubes } \frac{\pi \cdot d_{env} \cdot L_{tube}}{4} = \frac{4}{d_{env}} \quad (27)$$

Table 6  
Row correction factors when  $N_{row} < 20$  [47].

$N_{row}$	1	2	3	4	5	7
Staggered	0.64	0.76	0.84	0.89	0.92	0.95

$$a_s = \frac{4(1 - \varepsilon)}{d_{env.}}$$

The heat convection coefficient at the tube surface is estimated from Eq. (28) estimates the global convective heat transfer coefficient of the layer.

$$h_{env} = \frac{Nu \cdot k_f \cdot T_{avg}}{d_{env.}} \quad (28)$$

To calculate  $Nu$ , the HTF is assumed to be crossing a tube heat exchanger placed in staggered arrangements, where, similar assumption was validated experimentally by Zanganeh et al. [19]. The  $Nu$  is calculated at each raw from Zukauskas correlation Eq. (29) [51].

$$Nu = C_{row} \cdot C_{Re} \cdot Re_{max}^m \cdot Pr_{f,avg}^{0.36} \cdot \left( \frac{Pr_{f,avg}}{Pr_{f,m}} \right)^{0.25} \quad (29)$$

$$v_{f,max} = v_f \frac{S_T}{S_T - d_{env.}}, Re_{max} = \frac{\rho_f d_{env} v_{f,max}}{\mu_f}$$

$Re_{max}$  for this work is between 466 and 871, therefore, the value of  $C_{Re}$  and  $m$  is 0.51, 0.5, respectively.  $S_T$  is the distance between two consecutive tubes in the same row. The row correction factor is calculated at each raw according the factor lists illustrated in Table 6 provided by Incropera [47].

In the D—C approach according to Wakao [52], the HTF axial-effective thermal conductivity  $k_{f-ax}$  Eq. (30), includes a static and dynamic expressions. The static effective thermal conductivity on horizontal cylinder is calculated from Eq. (31), while dynamic HTF conductivity is calculated from Eq. (32) for  $Re > 0.8$ .

$$k_{f-ax} = k_f^0 + k_f^{dyn} \quad (30)$$

$$k_f^0 = \left( \frac{k_p}{k_f} \right)^{0.280 - 0.757 \log_{10} \left( \frac{k_p}{k_f} \right)} \quad (31)$$

$$k_f^{dyn} = 0.5 k_f \varepsilon Re \cdot Pe_f \quad Re > 0.8 \quad (32)$$

### 3.2.4. Initial conditions

For charge:

$$T_{PCM}^{(t=0)} = T_{pcm}^{(r_j,0)} = T_{initial}^{(t=0)} = T_{Low}$$

The liquid fraction

$$\lambda(r_j,0) = 0$$

For discharge at  $t = 0$ :

$$T_{PCM}^{(t=0)} = T_{pcm}^{(r_j,0)} = T_{initial}^{(t=0)} = T_{High}$$

The liquid fraction

$$\lambda(r_j,0) = 1$$

The boundary conditions at the center of the PCM tube is given by:

$$\frac{\partial T_p}{\partial r} = 0 \text{ at } r_i = 0$$

And the boundary conditions at the tube surface is given by Eq. (33) [53].

$$k_p \left( \frac{\partial T_{pcm,r}}{\partial r} \right)^n = h \left( T_f^{(n)} - T_{pcm}^{(R_{pcm},n)} \right) \quad (33)$$

## 3.3. Coupling the two models

### 3.3.1. Boundary conditions - charge

During charge according to Fig. 4, the simulation is firstly performed

in the D—C model (PCM layer), where the experimental hot oil temperature is applied as inlet boundary condition. Then the simulated output temperature of the HTF of the D—C is assumed to be the inlet temperature of HTF of the C—S model (the sensible heat part), where the HTF outlet temperature of the C—S model represents the tank's outlet temperature during charge, as follow:

In the D—C (PCM layer), hot HTF is injected at the top of the tank at:

$$T_{f,pcm}^{(1,n)} = T_{exp}^{(inlet,n)} = T_{Input}$$

While adiabatic boundary conditions are assumed at the inlet in the PCM layer and tank wall equations.

$$\frac{\partial T_{pcm}^{(1,n)}}{\partial z} = \frac{\partial T_w^{(1,n)}}{\partial z} = 0$$

The exit boundary condition is unknown, therefore no heat flux (adiabatic) boundary conditions are applied, in order to determine the last raw of the coefficients matrix [54]. The boundary condition at the PCM layer exit is adiabatic at  $j = H_{pcm}$  for the three equations:

$$\frac{\partial T_f^{(H_{pcm},n)}}{\partial z} = \frac{\partial T_{pcm}^{(H_{pcm},n)}}{\partial z} = \frac{\partial T_w^{(H_{pcm},n)}}{\partial z} = 0$$

The D—C approach is coupled with the C—S during charge process by assuming that outlet temperature for the D—C (PCM layer) is the input temperature of the C—S (sensible heat storage layer) at each modeled time step.

$$T_{f,pcm}^{(H_{pcm},n)} = T_{f,p}^{(1,n)}$$

Adiabatic boundary conditions are assumed in the energy balance equations of the solid filler and tank wall:

$$\frac{\partial T_p^{(1,n)}}{\partial z} = \frac{\partial T_w^{(1,n)}}{\partial z} = 0$$

Finally, at the outlet boundary condition of the C—S approach adiabatic conditions are implemented:

$$\frac{\partial T_f^{(H,n)}}{\partial z} = \frac{\partial T_p^{(H,n)}}{\partial z} = \frac{\partial T_w^{(H,n)}}{\partial z} = 0$$

### 3.3.2. Boundary conditions - discharge

During discharge the inverse of charge will happen (Fig. 4). The simulation starts in the C—S model (the sensible heat part), which uses the experimental cold oil temperature as the inlet boundary condition. Then the simulated HTF outlet temperature of the C—S model is assumed to be the HTF inlet temperature of the D—C model (the PCM layer). The HTF outlet temperature of the D—C model represent the outlet temperature of the tank during discharge, as follow:

$$T_{f,p}^{(1,n)} = T_{exp}^{(inlet,n)} = T_{Input}$$

The outlet temperature of the HTF resulting from C—S model is considered as the inlet temperature of the HTF in the D—C layer (PCM).

$$T_{f,p}^{(H_{p,n})} = T_{f,pcm}^{(1,n)}$$

### 3.3.3. Discretization

The Matlab® program uses the finite difference method that is implicit in time second order central differencing scheme. The simulation updates the thermophysical properties of the materials at each iteration.

The program solves three-coupled partial non-linear differential equations of both models C—S and D—C. It uses the Newton-Raphson iteration method with convergence criteria of  $10^{-4}$ , and a time step of  $\Delta t = 0.5$  s. The size of the control volume in the C—S model is  $\Delta z = 0.02$  m [55], while the control volume in the D—C is equal to the capsule diameter 48.3 mm and the number of radial components is 10 [56] as depicted in Fig. 10.

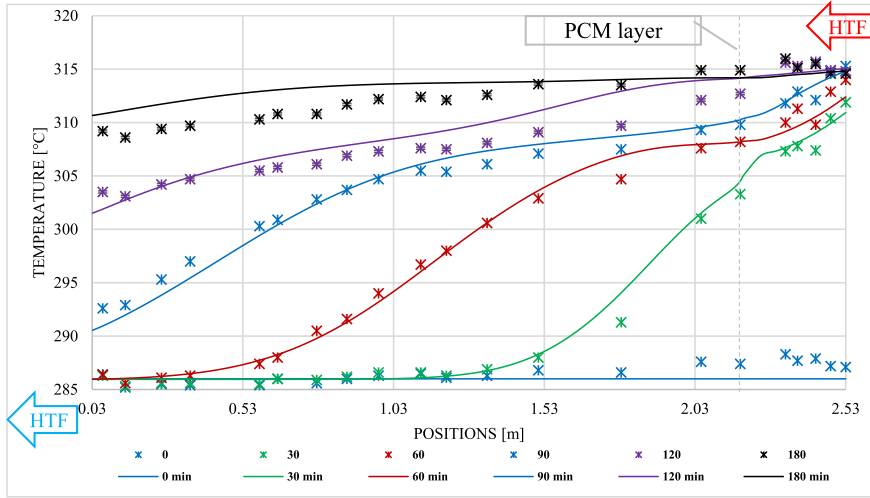


Fig. 11. Temperature profile of the charge process, model against experiment.

## 4. Results

### 4.1. Charging process

The charging process starts when all mediums inside the tank have about the same low temperature  $T_{low} = 286$  [°C]. While the HTF is injected at a constant mass flow rate of 2700 kg/h the top of the tank, with a temperature increasing gradually from  $T_{low}$  to  $T_{high} = 315$  °C using the electrical heater, then it remains constant at  $T_{high}$  until the end of the process.

During this process Fig. 11, the hot oil enters the top of the tank from the right of figure charging the PCM layer at the top of the tank between the thermocouples located at 2.53 m – 2.18 m. After, it charges the alumina sphere from top to bottom between position 2.18 m down to 0.05 m above the tank's outlet, where the cold oil exits the tank from the left of the Figure. The temperature profiles are plotted each 30 min from 0 to 180 min.

The charging experimental temperature profile of points in Fig. 11 illustrates that:

- After 30 min of charge the oil is at 310 °C at the tank's inlet (PCM layer inlet), while the oil temperature in the middle of the PCM layer section demonstrates a constant value around 307 °C. This semi-

plateau behavior can be attributed to the beginning of phase changing of the PCM within the tubes, where the melting temperature of the  $\text{NaNO}_3$  is about 307 °C according to the DCS measurements of this work (Section 2.3 above). In the sensible heat section of the tank, most of the alumina spheres are still at  $T_{low}$ .

- After 60 min of charge, the tank's inlet temperature reaches 315 °C; the maximum temperature of this process, the rate of increase of the HTF temperature in the PCM layer is slower than the SHSM layer affected by the melting of the remaining PCM within the tubes. Furthermore, about third of the alumina spheres is charged above 300 °C between thermocouples at 1.34 m – 2.05 m. While the HTF temperature at the tank's outlet remains at the lowest temperature of this operation 285 °C.
- At 90 min of charge, the HTF temperature in the PCM layer exceeded 310 °C, which suggests that most of the PCM had been melted. Moreover, about two third of the SHSM layer is charged above 300 °C between 0.585 m – 2.05 m, and the tank's outlet temperature started to increase.
- From 120 min until 180 min, both mediums continue to charge at similar rate, the tank's outlet temperature increases to near the  $T_{high}$ , where the process stopped.

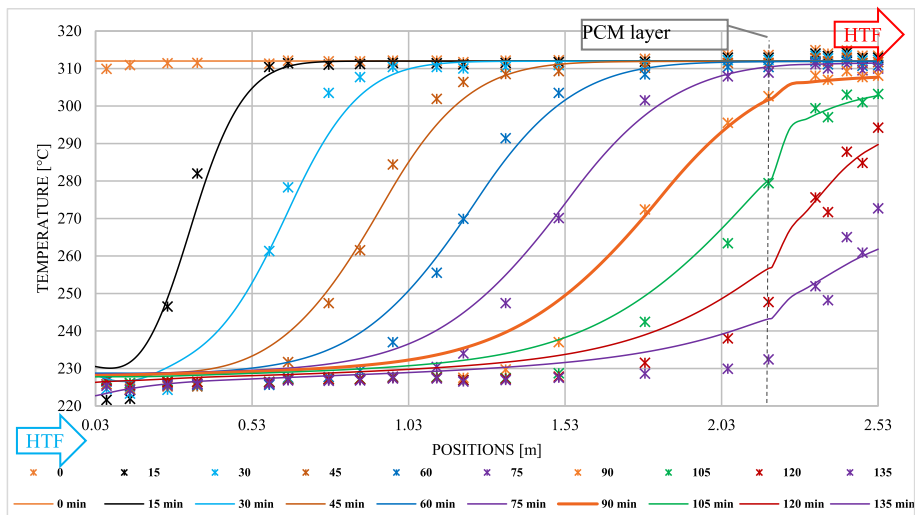


Fig. 12. Temperature profile of the discharge process, model against experiment.

#### 4.2. Discharging process

During the discharge Fig. 12 points temperature profile, all the mediums inside the thermocline are at  $T_{high}$  312 °C, while the HTF is entering the tank at  $T_{low}$  226 °C with a constant mass flow rate 2000 kg/h. The cold oil is injected from the tank's lowest point (the left side of figure), discharging the alumina spheres section from the tank between the thermocouples located at 0.05 m up to 2.18 m. Then the HTF enters the PCM layer immediately after the thermocouple placed at 2.18 m height, and exits the PCM layer and the tank after the thermocouple at 2.53 m (the right side of the Figure). Temperatures profiles are plotted from 0 min up to 135 min at 15 min intervals.

The discharging experimental temperature profile of points in Fig. 11 shows that:

- After 75 min of discharge, about 50% of the alumina spheres section of the tank is at the low temperature  $T_{low}$  between thermocouples at 0.05 m – 1.08 m, which indicates that about 50% of the energy of the SHSM is discharged.
- At 90 min the temperature profile indicates that significant amount of the energy of the alumina spheres has been already discharged. While the temperatures of the HTF between the PCM tubes demonstrate a constant temperature at about 306 °C, which is very near the solidification temperature found during the DSC analysis of the  $NaNO_3$  304.5 °C (2.3 above). This indicates that the PCM experiences an isothermal solidification at this time of the discharge.
- After 105 min of discharge, the SHSM has nearly no more energy to discharge since most of the materials having reached the  $T_{low}$  of the experiment. On the other hand, the HTF temperature between the PCM tubes shows quasi-constant values at a level lower than the previous step at about 300 °C. This can be attributed to the existence of some PCM in phase changing state. Nevertheless, the already solidified amount PCM inside the tubes limiting the heat exchange to the outside HTF due to its low thermal resistance.
- Between 120 min and 135 min, the end of the discharge, the temperature profiles show a reduced HTF temperature inside the tank in both the PCM layer and the SHSM.

#### 4.3. Radial temperature distribution in the PCM layer

The radial temperature evolution within the PCM layer is analyzed by plotting the temperatures obtained from the horizontal thermocouples located within the PCM layer. These thermocouples are located at six locations as illustrated in Fig. 4.

Fig. 13 plots the radial temperature evolution during the charge process at the designated positions. The thermocouples data demonstrate a homogeneous HTF temperature distribution along the tank's radial direction, which supports the assumption of one-dimensional behavior for the model. A small fluctuation in the temperature is observed for thermocouples located at 2.18 m, which is located in between the PCM layer and the alumina spheres bed. This deviation can be explained by the variation of HTF velocity distribution between two different filler materials, the alumina spheres and  $NaNO_3$  tubes.

Similar to the charge process, the radial temperature evolution maintained a one-dimensional evaluation during the discharge as shown in Fig. 14. Furthermore, a small deviation in the radial temperature distribution is observed at the interface position between the PCM tubes and alumina spheres.

#### 4.4. Stand-by

To evaluate the thermal behavior of the TES tank during a stand-by, the system is partially discharged from 310 °C to 220 °C and the operation is intentionally stopped while the PCM layer temperatures is about 310 °C, and most of the remaining storage is at the low temperature.

Fig. 15 plots the temperature profile inside the tank during this

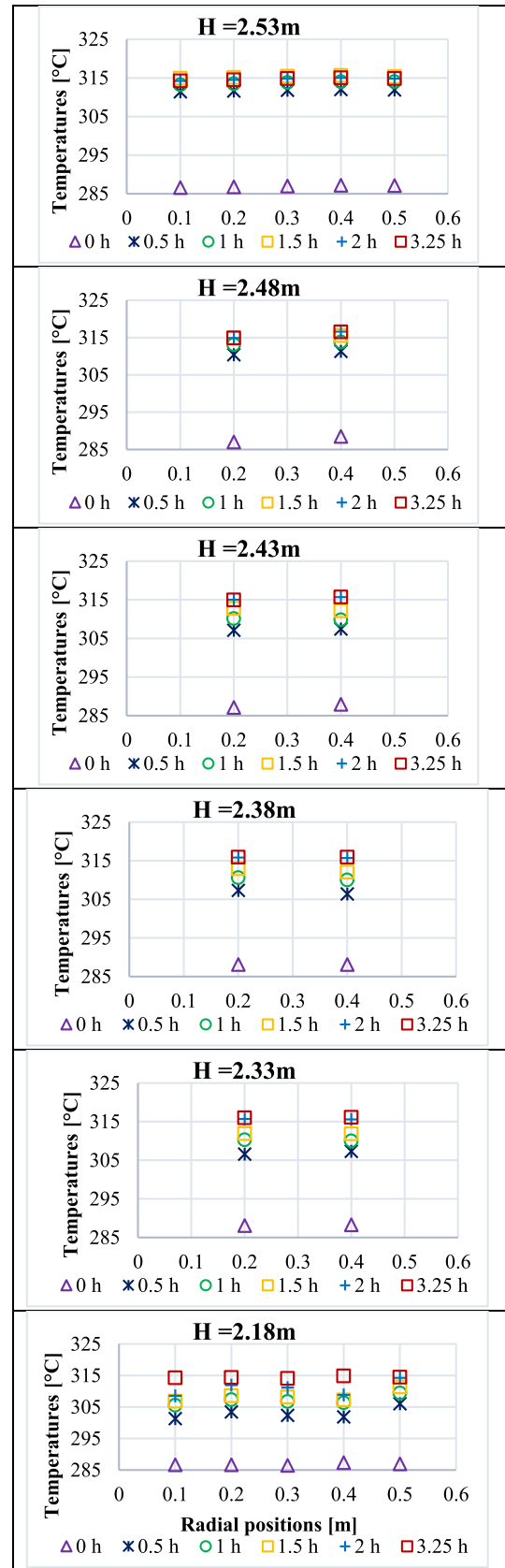


Fig. 13. Radial temperature evolution during the charge at six axial reference positions.

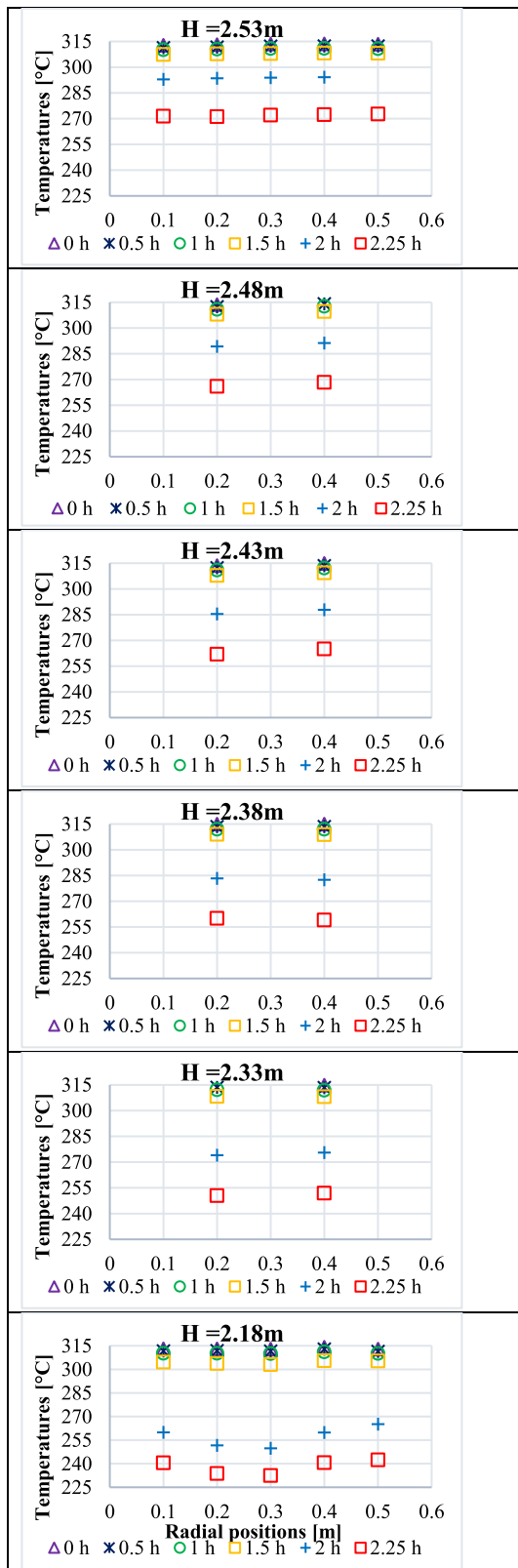


Fig. 14. Radial temperature evolution during the discharge at six axial reference positions.

stand-by period of about 5 h. Three main regions can be identified, low temperature, thermal gradient, and high temperature regions.

The low-temperature zone covers about 60% of tank's height from the lowest point up to 1.53 m, which is all in the sensible heat storage

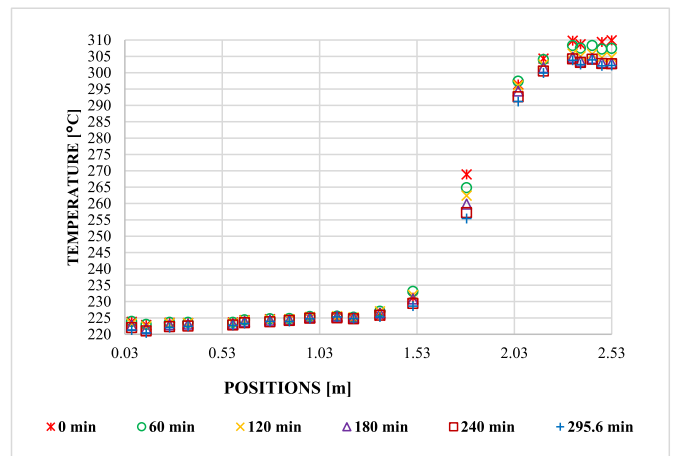


Fig. 15. Temperature profile during a stand-by period of 5 h.

part. The temperature remained unchanged for the 5 h test about 225 °C.

The thermal gradient region (thermocline thickness) occupies about 25.7% of the tank's height from 1.53 m up to 2.18 m with a temperature ranging from 225 to 300 °C, which is also located in the sensible heat storage part up to the PCM layer inlet. The lower end of this region has a stable temperature of approximately 230 °C for the test duration, while the upper end has also a stable temperature of ~300 °C. However, in between these two limits, the farther the point from the PCM the higher the temperature drop from its initial temperature, 5 °C at 2.05 m and 13 °C at 1.8 m, which indicates that the PCM solidification in the above region reduced the temperature drop in the area adjacent to the PCM.

The high temperature zone represents 14.3% of the tank's height, where the temperature drops for about 4 °C, from 310 °C down to 306 °C in the first hour, and from 306 °C down to 302 °C for the second hour, then it remains stable at 302 °C for the next 4 h until the end of the test.

This observation indicates that the solidification is happening during stand-by, but with a lower kinetics compared to charge and discharge. Where the temperature drops inside the tank during the stand-by due to thermal stratification inside the tank and the thermal losses to the environment, when the HTF temperature in the PCM layer drops to below the solidification point of the NaNO<sub>3</sub>, some of the PCM starts to solidify and stabilizing the temperature due to the latent heat of fusion. The low thermal conductivity of the solid PCM limits the heat transfer rate between liquid and solid PCM, resulting in slow solidification over time, consequently slow temperature drop at the tube surface as well as HTF in the adjacent area to the tubes.

The practice of partially discharging the combined thermal energy storage is not recommended because it implies losing the latent heat of fusion of the PCM in non-production operation.

#### 4.5. Model validation

The temperature profiles is chosen to validate the model because it represents the dynamic response of the TES at multiple time steps, which embedding the complex heat transfer phenomena within the tank. It provides an illustration about the temperature gradient and thermal stratification within the tank [57], as well as the level of stored and discharged thermal energy [58].

Fig. 11 compares the predicted temperature profile along the axial axis of the tank to the experimental results during the charge process, solid lines and points, respectively. The model presents a good prediction of the experimental temperature profiles, although small deviation appears at some points, which can be accommodated with the  $\pm 2.7$  °C related to the 13% uncertainty of the measurement (2.6 above). The PCM's influence is observed in the experiment and the simulation at about 307 °C after 30 min of charge, which is very near the melting

temperature of the NaNO<sub>3</sub>.

Fig. 12 compares the numerical temperature profiles against the experimental ones during discharge, solid lines and points, respectively. It illustrates that, computed temperature profiles during discharge have an acceptable agreement with the experimental temperatures in general. The effects of PCM solidification is evidenced on the HTF temperature for temperature profiles related to discharge times longer or equal to 90 min. The model demonstrated some deviation from the experimental results between 120 min and 135 min the end of the discharge, which could be attributed to the unstable mass flow rate as well as lower HTF inlet temperature in the experimental setting at the final discharge stage.

The overall thermal dispersion along the tank vertical axis comes from complex thermal interaction between the three components HTF, tank's wall, and the solid filler material. The main heat transfer means are conduction between the solid fillers, wall to solid filler conduction, the temperature gradient within the solid filler, dispersion within the HTF, convection (HTF to the wall), convection between HTF to solid filler, and convection at the wall to the outside environment. Furthermore, when PCM is used as in this work, the melting/solidification and the natural convection of the PCM are added factors to the complexity of modelling the overall thermal dispersion inside the tank.

These phenomena are very hard to be experimentally separated from each other at this size of tank as well as in real case scenario, hence, the general thermal behavior of the HTF can only be followed and evaluated. In any case, the model consistently provides similar HTF temperatures profiles as the experimental ones at multiple time steps and locations inside the tank for both charge Fig. 11 and discharge Fig. 12. The similar shapes and behavior of the temperature profiles confirm that the model is adequately valid for both charge and discharge operations.

#### 4.6. Estimation of liquid fraction in PCM

One advantage of using enthalpy porosity method is the ability to predict liquid fraction. This parameter indicates the status of the PCM charge at the studied control volume Fig. 16. Where charged PCM is represented by liquid fraction of one and the PCM at liquid status. While discharged PCM is described by liquid fraction of zero where the PCM is at solid status. When the studied control volume has the two phases it is characterized by liquid fraction between zero and one, which illustrates the PCM charge percentage.

On the other hand, the liquid fraction is not a quantitative parameter, because the model is 1D with a lot of simplifying assumptions, beside the complex geometry of the PCM tubes. Therefore, its value cannot describe the actual status of the PCM, while it is used in this section just as an indication of the PCM charge status.

During charge process, the liquid fraction is evaluated at the last tube in the PCM layer illustrated in Fig. 17.

Fig. 18 (a) plots the liquid fraction against the ten control volumes of the tube radius after 120 min of charge. It illustrates that the liquid fraction at PCM layer exit is equal to one, which confirms that the PCM is entirely melted in this row, consequently all the PCM at previous rows had been melted. This could be supported from the temperature profile during charge at 120 min (Fig. 11) where the HTF temperature is already exceeded the PCM phase changing temperature of 307 °C, which

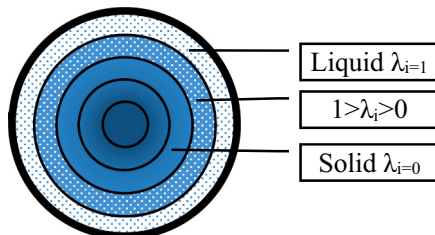


Fig. 16. Liquid fraction distribution along the control volume.

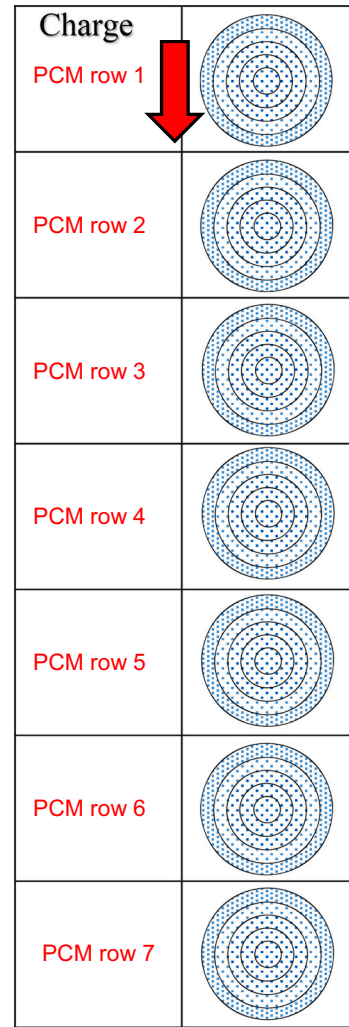


Fig. 17. Liquid fraction within control volumes of the PCM Layer in the 1D model during charge.

indicates that the PCM has completed the melting.

While during discharge process, the liquid fraction is checked at all seven control volumes of the PCM layer Fig. 19.

Fig. 18 (b) plots the predicted liquid fractions at all PCM rows at 105 min. It shows that rows from 3 to 7 have a potential of more than 50% of their PCM is still in liquid phase, which indicates that the PCM is not completely solidified in all tubes. Moreover, the HTF temperature profile at this time step during discharge Fig. 12 indicates similar behavior at 105 min. It shows a semi-plateau curve at a lower temperature than the PCM solidification at 300 °C, which is an indication of the existence of PCM still undergoing the solidification process. Therefore, this observation also indicates an additional potential energy that could be used to increase the discharge duration and efficiency. However, the heat transfer coefficient should be improved within the solid PCM and the tubes envelop using a suitable solution such as improving the thermal conductivity of the PCM, using nanomaterials, and metal fins within the tubes.

## 5. Conclusions

This work developed a one-tank TES that combines a layer of tube-encapsulated PCM at its top to a sensible heat storage medium bed. The pilot-scale TES of MICROSOL-R installation at PROMES-CNRS, France research facility is used to perform the experimental part of this study.

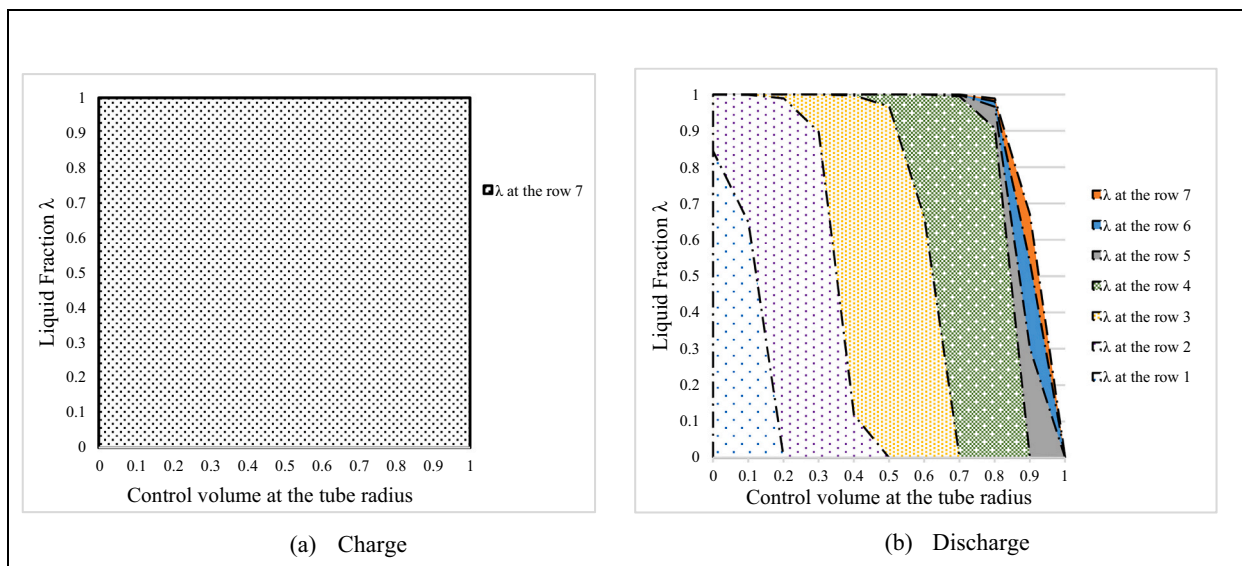


Fig. 18. Estimated Liquid fraction snap shot (a) charge at 120 min (b) discharge at 105 min.

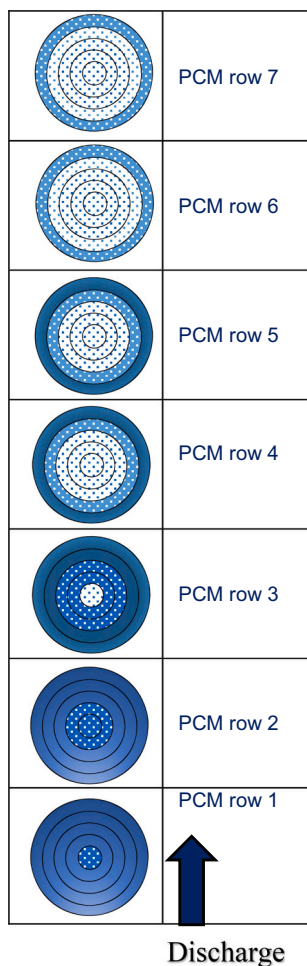


Fig. 19. Liquid fraction within control volumes of the PCM Layer in the 1D model during discharge.

The experiment uses Jarytherm® oil as HTF, 4.41 ton of alumina spheres as a sensible heat storage material, and  $\text{NaNO}_3$  as PCM that fills about 5.5 vol% of the TES storage tank volume. The PCM layer consists

of 140 stainless steel filled with about 86%  $\text{NaNO}_3$ , an air gap of 14% in each tube is left to accommodate the PCM volume changes during melting without stressing the tube's wall. The final mass of  $\text{NaNO}_3$  that filled the tubes is 337 kg, while the stainless steel envelope weighted about 243 kg.

During charge, the experimental HTF temperature profile shows a semi-constant region at 307 °C at 30 min. During the discharge of the TES, the influence of PCM solidification is illustrated at 306 °C after 90 min, this temperature is also near the phase change temperature of the PCM measured by the DCS test.

Furthermore, another semi-plateau temperature appeared on the profile of the HTF at 300 °C after 105 min that is below the phase changing point of the PCM. This suggests that while there is still liquid PCM undergoing phase change inside the tubes, the already solidified PCM is limiting the heat transfer between the liquid PCM and its stainless steel envelop, reducing the HTF temperature near the PCM encapsulation, and limiting the efficiency of the process.

The model that couples C—S approach in the SHSM and D—C in the PCM layer is validated from the experimental results. The predicted HTF temperature profiles agrees satisfactorily with experimental data, for both charge and discharge. Furthermore, the 1D thermal behavior of the HTF is verified from the radial temperatures.

It could be inferred from the numerical estimation of the liquid fraction during discharge that a significant amount of PCM is still in liquid phase. Which is undesired during the operation, therefore it is necessary to improve the thermal performance of the PCM layer by increasing the heat transfer between the PCM and HTF, using a proper method.

Ongoing work is on progress to develop a general sizing method to the PCM layer to improve the thermal performance of the TES, evaluate the thermal performance of the combined TES versus a sensible heat storage material only case for the same storage size and operating conditions.

#### CRedit authorship contribution statement

**M.A. Keilany:** Data curation, Formal analysis, Investigation, Methodology, Project administration, Resources, Software, Validation, Visualization, Writing – original draft, Writing – review & editing. **S. Vannerem:** Data curation. **M. Milhé:** Formal analysis, Methodology, Software, Supervision, Validation, Writing – review & editing. **Q. Falcoz:** Formal analysis, Methodology, Resources, Supervision, Validation,

Writing – review & editing. **J.-J. Bézian**: Conceptualization, Formal analysis, Funding acquisition, Methodology, Project administration, Validation, Writing – review & editing. **G. Flamant**: Conceptualization, Formal analysis, Funding acquisition, Methodology, Project administration, Validation, Writing – review & editing.

### Declaration of competing interest

The authors declare that they have no known competing financial interests or personal relationships that could have appeared to influence the work reported in this paper.

### Acknowledgments

This work was supported by the French “Investments for the Future” program managed by the National Agency for Research under contract ANR-10-LABX-22-01 (LABEX SOLSTICE) and ANR-10-EQPX-49 (Equipex SOCRATE).

The authors acknowledge Celine Boachon and Nicolas Bouillet for their technical assistance during tests.

### References

- [1] X. Py, N. Sadiki, R. Olives, V. Goetz, Q. Falcoz, Thermal energy storage for CSP (concentrating solar power), EPJ Web Conf. 148 (2017) 1–24.
- [2] U. Pelay, L. Luo, Y. Fan, D. Stitou, M. Rood, Thermal energy storage systems for concentrated solar power plants, Renew. Sustain. Energy Rev. 79 (March 2016) (2017) 82–100.
- [3] S. Kuravi, J. Trahan, D.Y. Goswami, M.M. Rahman, E.K. Stefanakos, Thermal energy storage technologies and systems for concentrating solar power plants, Prog. Energy Combust. Sci. 39 (4) (2013) 285–319.
- [4] J.E. Pacheco, S.K. Showalter, W.J. Kolb, Development of a molten-salt thermocline thermal storage system for parabolic trough plants, J. Sol. Energy Eng. 124 (2) (2002) 153–159.
- [5] M.A. Keilany, M. Milhé, J. Bézian, Q. Falcoz, G. Flamant, Experimental evaluation of vitrified waste as solid fillers used in thermocline thermal energy storage with parametric analysis, J. Energy Storage 29 (February) (2020), 101285.
- [6] C. Xu, Z. Wang, Y. He, X. Li, F. Bai, Sensitivity analysis of the numerical study on the thermal performance of a packed-bed molten salt thermocline thermal storage system, Appl. Energy 92 (2012) 65–75.
- [7] M. Faraji, H. El Qarnia, E.K. Lakhali, Thermal analysis of a phase change material based heat sink for cooling protruding electronic chips, J. Therm. Sci. 18 (3) (2009) 268–275.
- [8] H. Mehling, L.F. Cabeza, Heat and Cold Storage With PCM, Springer, Berlin Heidelberg, 2008.
- [9] A. Lazrak, J.F. Fourmigué, J.F. Robin, An innovative practical battery thermal management system based on phase change materials: numerical and experimental investigations, Appl. Therm. Eng. 128 (2018) 20–32.
- [10] V. Kapsalis, D. Karamanis, Solar thermal energy storage and heat pumps with phase change materials, Appl. Therm. Eng. 99 (2016) 1212–1224.
- [11] H. Nazir, et al., Recent developments in phase change materials for energy storage applications: a review, Int. J. Heat Mass Transf. 129 (2019) 491–523.
- [12] G. Zanganeh, M. Commerford, A. Haselbacher, A. Pedretti, A. Steinfeld, Stabilization of the outflow temperature of a packed-bed thermal energy storage by combining rocks with phase change materials, Appl. Therm. Eng. 70 (1) (2014) 316–320.
- [13] N. Ahmed, K.E. Elfeky, L. Lu, Q.W. Wang, Thermal and economic evaluation of thermocline combined sensible-latent heat thermal energy storage system for medium temperature applications, Energy Convers. Manag. 189 (March) (2019) 14–23.
- [14] A.B. Hernández, I. Ortega-Fernández, I. Uriz, A. Ortuondo, I. Loroño, J. Rodríguez-Aseguinolaza, Parametric analysis and optimization of a combined latent-sensible packed bed energy storage system, AIP Conf. Proc. (2018), <https://doi.org/10.1063/1.5067106>, 2033(November).
- [15] P.A. Galione, C.D. Pérez-Segarra, I. Rodríguez, O. Lehmkühl, J. Rigola, A new thermocline-PCM thermal storage concept for CSP plants. Numerical analysis and perspectives, Energy Procedia 49 (2014) 790–799.
- [16] P.A. Galione, C.D. Pérez-Segarra, I. Rodríguez, A. Oliva, J. Rigola, Multi-layered solid-PCM thermocline thermal storage concept for CSP plants. Numerical analysis and perspectives, Appl. Energy 142 (2015) 337–351.
- [17] P.A. Galione, C.D. Pérez-Segarra, I. Rodríguez, S. Torras, J. Rigola, Multi-layered solid-PCM thermocline thermal storage for CSP. Numerical evaluation of its application in a 50MWe plant, Sol. Energy 119 (2015) 134–150.
- [18] B. Zhao, M. Cheng, C. Liu, Z. Dai, An efficient tank size estimation strategy for packed-bed thermocline thermal energy storage systems for concentrated solar power, Sol. Energy 153 (2017) 104–114.
- [19] G. Zanganeh, R. Khanna, C. Walser, A. Pedretti, A. Haselbacher, A. Steinfeld, Experimental and numerical investigation of combined sensible-latent heat for thermal energy storage at 575 deg C and above, Sol. Energy 114 (2015) 77–90.
- [20] V.R. Voller, Fast implicit finite-difference method for the analysis of phase change problems, Numer. Heat Transf. 17 (September 2012) (1990) 155–169.
- [21] T. Fasquelle, Q. Falcoz, P. Neveu, F. Lecat, N. Bouillet, G. Flamant, Operating results of a thermocline thermal energy storage included in a parabolic trough mini power plant, AIP Conf. Proc. 1850 (2017).
- [22] S.A. Mohamed, et al., A review on current status and challenges of inorganic phase change materials for thermal energy storage systems, Renew. Sustain. Energy Rev. 70 (December 2016) (2017) 1072–1089.
- [23] S. Pincemin, R. Olives, X. Py, M. Christ, Highly conductive composites made of phase change materials and graphite for thermal storage, Sol. Energy Mater. Sol. Cells 92 (6) (2008) 603–613.
- [24] E. Rojas, R. Bayón, E. Zarza, Liquid crystals: a different approach for storing latent energy in a DSG plant, Energy Procedia 69 (2015) 1014–1022.
- [25] M. Liu, et al., Review on concentrating solar power plants and new developments in high temperature thermal energy storage technologies, Renew. Sust. Energy Rev. 53 (2016) 1411–1432.
- [26] A.F. Regin, S.C. Solanki, J.S. Saini, Heat transfer characteristics of thermal energy storage system using PCM capsules: a review, Renew. Sust. Energy Rev. 12 (9) (2008) 2438–2451.
- [27] R. Jacob, F. Bruno, Review on shell materials used in the encapsulation of phase change materials for high temperature thermal energy storage, Renew. Sust. Energy Rev. 48 (2015) 79–87.
- [28] P.B. Salunkhe, P.S. Shembekar, A review on effect of phase change material encapsulation on the thermal performance of a system, Renew. Sust. Energy Rev. 16 (8) (2012) 5603–5616.
- [29] S.H. Goods, R.W. Bradshaw, Corrosion of stainless steels and carbon steel by molten mixtures of commercial nitrate salts, ASM Int. 13 (February) (2003) 78–87.
- [30] T.E. Alam, J.S. Dhau, D.Y. Goswami, E. Stefanakos, Macroencapsulation and characterization of phase change materials for latent heat thermal energy storage systems, Appl. Energy 154 (2015) 92–101.
- [31] M. Munro, Evaluated material properties for a sintered alpha-alumina, J. Am. Ceram. Soc. 80 (8) (2005) 1919–1928.
- [32] R. Anderson, S. Shiri, H. Bindra, J.F. Morris, Experimental results and modeling of energy storage and recovery in a packed bed of alumina particles, Appl. Energy 119 (2014) 521–529.
- [33] S. Bellan, et al., Numerical analysis of charging and discharging performance of a thermal energy storage system with encapsulated phase change material, Appl. Therm. Eng. 71 (1) (2014) 481–500.
- [34] Martin Marietta Aerospace, in: Sandia Report: Molten Salt Safety Study, 1980, pp. 1–29.
- [35] J. Carvill, Mechanical Engineer's Data Handbook, 1993.
- [36] D.V. Hale, M.J. Hoover, M.J.O. Neill, Phase Change Materials Handbook by NASA Contractor Report NASA CR-51363 232, 1971.
- [37] G.J. Janz, C.B. Allen, N.P. Bansal, R.M. Murphy, R.P.T. Tomkins, Physical Properties data compilations relevant to energy storage, in: Secretary of Commerce U.S. Government, 1979, p. 449.
- [38] T. Bauer, D. Laing, R. Tamme, Characterization of sodium nitrate as phase change material, Int. J. Thermophys. 33 (1) (2012) 91–104.
- [39] T.E. Alam, J. Dhau, D.Y. Goswami, M.M. Rahman, E. Stefanakos, in: Imece2014-38307 Experimental Investigation of a Packed-Bed Latent Heat Thermal, 2014, pp. 1–6.
- [40] A. Bruch, J.F. Fourmigué, R. Couturier, Experimental and numerical investigation of a pilot-scale thermal oil packed bed thermal storage system for CSP power plant, Sol. Energy 105 (2014) 116–125.
- [41] N. Wakao, S. Kagueli, T. Funazkri, Effect of fluid dispersion coefficients particle-to-fluid heat transfer coefficients in packed beds, Chem. Eng. Sci. 34 (3) (1978) 325–336.
- [42] E. Achenbach, Heat and flow characteristics of packed beds, Exp. Thermal Fluid Sci. 10 (1) (1995) 17–27.
- [43] S. Bu, J. Yang, Q. Dong, Q. Wang, Experimental study of flow transitions in structured packed beds of spheres with electrochemical technique, Exp. Therm. Fluid Sci. 60 (150) (2015) 106–114.
- [44] V. Palomba, A. Frazzica, Application of numerical methods for the design of thermocline thermal energy storage: literature review and critical analysis, J. Energy Storage 46 (December 2021) (2022) 103875.
- [45] D. Kunii, J.M. Smith, Heat transfer characteristics of porous rocks, AIChE J. 6 (1) (1960) 71–78.
- [46] J. Beek, Design of packed catalytic reactors, Adv. Chem. Eng. 3 (C) (1962) 203–271.
- [47] F.P. Incropera, D.P. DeWitt, T.L. Bergman, A.S. Lavine, Fundamentals of Heat and Mass Transfer, 2007.
- [48] S.W. Churchill, H.H.S. Chu, Correlating equations for laminar and turbulent free convection from a vertical plate, Int. J. Heat Mass Transf. 18 (11) (1975) 1323–1329.
- [49] M. Wu, C. Xu, Y.-L. He, Dynamic thermal performance analysis of a molten-salt packed-bed thermal energy storage system using PCM capsules, Appl. Energy 121 (2014) 184–195.
- [50] A. Prasad, S. Sengupta, Nusselt number and melt time correlations for melting inside a horizontal cylinder subjected to an isothermal wall temperature condition, J. Sol. Energy Eng. 110 (4) (1988) 340.
- [51] A. Žukauskas, Advances in heat transfer volume 8, Adv. Heat Transf. 8 (1972) 93–160.
- [52] N. Wakao, S. Kagueli, Heat and mass transfer in packed beds, Am. Inst. Chem. Eng. 29 (6) (1983).

- [53] K.E. Elfeky, N. Ahmed, Q. Wang, Numerical comparison between single PCM and multi-stage PCM based high temperature thermal energy storage for CSP tower plants, *Appl. Therm. Eng.* 139 (February) (2018) 609–622.
- [54] G. Strang, *Computational Science and Engineering*, Wellesley-Cambridge Press, Wellesley, MA, 2007.
- [55] J.F. Hoffmann, T. Fasquelle, V. Goetz, X. Py, A thermocline thermal energy storage system with filler materials for concentrated solar power plants: experimental data and numerical model sensitivity to different experimental tank scales, *Appl. Therm. Eng.* 100 (2016) 753–761.
- [56] K. Nithyanandam, R. Pitchumani, A. Mathur, Analysis of a latent thermocline storage system with encapsulated phase change materials for concentrating solar power, *Appl. Energy* 113 (2014) 1446–1460.
- [57] J. Duffie, W. Beckman, *Solar Engineering of Thermal Processes* 4th ed., 116, 2013.
- [58] M.S. Abdel-Salam, S.L. Aly, A.I. El-Sharkawy, Z. Abdel-Rehim, Thermal characteristics of packed bed storage system, *Int. J. Energy Res.* 15 (1) (1991) 19–29.